Three-dimensional time-lapse velocity tomography of an underground longwall panel

Kray Luxbacher[a], Erik Westman[a], Peter Swanson[b], Mario Karfakis[a]

[a]*Department of Mining & Minerals Engineering, Virginia Tech., Blacksburg, VA 24061-0239, USA*
[b]*Spokane Research Laboratory, National Institute for Occupational Safety and Health, Spokane, WA 99207, USA*

Abstract

Three-dimensional velocity tomograms were generated to image the stress redistribution around an underground coal longwall panel to produce a better understanding of the mechanisms that lead to ground failure, especially rockbursts. Mining-induced microseismic events provided passive sources for the three-dimensional velocity tomography. Surface-mounted geophones monitored microseismic activity for 18 days. Eighteen tomograms were generated and high-velocity regions correlated with high abutment stresses predicted by numerical modeling. Additionally, the high-velocity regions were observed to redistribute as the longwall face retreated, indicating that velocity tomography may be an appropriate technology for monitoring stress redistribution in underground mines.

Keywords: Rockbursts; Longwall; Coal; Tomography; Velocity; Stress

1. Introduction

Roof characterization and control pose significant challenges to the underground mining industry. Approximately one-third of fatalities reported in underground mines in the United States between 2001 and 2005 were the result of fall of roof, rib, or face [1]. In addition to accounting for a significant portion of fatal accidents, these incidents also result in a considerable portion of lost time injuries, translating into substantial losses in production.

Some of the most unpredictable and violent types of roof failure are rockbursts, often referred to in coal mines as bumps or bounces. Rockbursts are sudden and violent failures of overstressed rock that can cause expulsion of material and airblasts. Rockbursts not only pose a danger to miners due to flying material, but they can cause ventilation changes, and may also propagate dust and gas into the air, creating a potentially explosive environment [2]. Rockbursts and bumps generally occur in mines that have at least 300 m (about 1000 ft) of cover and are either overlain or underlain by a massive and competent geologic formation [2,3].

Velocity tomography is a technology that can be used to ascertain the relative state of stress and the redistribution of stress in a rock mass. Velocity tomography relies on the transmission of seismic waves, specifically p-waves, through a rock mass. The velocity of the wave is determined, and the mass is divided into voxels, or cubes, with a velocity calculated for each cube. The sharpness of the image is dependent on the size of the voxel. The voxel size must be optimized to insure that all voxels are traversed by a sufficient number of rays.

Velocity tomography is useful for inferring stress redistribution. During the pre-failure regime, the p-wave velocity usually increases linearly with stress at lower stress levels, and then plateaus at higher stress levels. This increase of p-wave velocity with stress is attributed to the closure of cracks and pore space [4–8]. With increasing levels of structural damage, the p-wave velocity can drop to values less than observed in the initial state.

In order to implement velocity tomography, a source must be selected for the seismic waves. Sources may be active or passive. Active sources, such as hammer strikes,

blasts, or cutting equipment are advantageous because they allow for consistent and predictable seismic raypath distribution. However, active sources are not always feasible for relatively long time-lapse studies, since they usually require the presence of a person to initiate the source and record the time and location. Passive sources allow for remote, continuous monitoring of a rock mass. However, they are also associated with a unique set of challenges, including accurate source location and inadequate or irregular raypath density. Mining-induced microseismic events are well suited for utilization as passive sources in velocity tomography. The events are usually located in areas of active mining that are the target areas for velocity tomography. Microseismic events in active mining areas are frequent enough to allow for adequate raypath density. Numerous studies have shown that analyses of microseismic activity provides insight into ground failure processes [9–11]. Microseismic sources allow for noninvasive, remote time-lapse monitoring over a period of days, weeks, or even months.

The site chosen for this study was an underground longwall coal mine. A retreating longwall panel was monitored for 18 days. The site has considerable microseismic activity, making it ideal for passive source velocity tomography.

2. Tomography

Tomography has become an essential diagnostic tool in the medical industry; a CAT-scan, computer-assisted tomography, is one example [12]. Tomography also has many geotechnical applications including study of faults and ore body delineation [13,14]. Tomography has been applied as a tool for imaging stress in laboratory rock specimens [15–17] and in underground mines with moderate success.

Stress distribution in numerous underground structures has been imaged, including pillars, tunnels, and longwall panels. Pillars have been studied extensively due to their relatively small scale and predictable stress concentrations. Friedel et al. conducted active source imaging of the footprint left by two coal pillars on the mine floor, determining that velocity increased as the face approached the pillar and that velocity decreases around the pillar edge corresponded with failure due to spalling [18]. Active source imaging has been implemented for pillar tomography at Homestake Mine [19], and at Edgar Experimental Mine [20]. Watanabe and Sassa also used active sources to image both a pillar and a triangular area between two drifts [21], while Manthei used active source geometry to image pillars in a potash mine [22].

Tunnels have also been studied extensively to determine stress redistribution around openings. Many of these studies have been conducted at the Underground Research Laboratory (URL) in Canada; passive source [23,24] and active source studies [17] of tunnels at the URL can be found in the literature.

Tunnel and pillar studies are relatively simple since the small-scale geometry allows for optimum source and receiver placement. Larger scale studies are more difficult to design, but have been conducted successfully. Körmendi et al. used in-seam receivers with active source geometry for a longwall panel in an underground coal mine, and found that high-velocity areas advanced with the face and were typical of stress redistribution encountered on a longwall [25]. Active source tomograms have been compared to "simulated passive source" tomograms [26]. Active sources have been used in metal mines, and high-velocity areas were imaged ahead of working faces [24,27]. A longwall shearer provided an active source to produce tomograms of a longwall panel showing high-stress areas from mid-face towards the tailgate [28]. No long-term time-lapse studies utilizing passive sources are found in the literature.

Velocity tomography relies on a simple relationship, that the velocity along a seismic ray is the raypath distance divided by the time to travel between the source and receiver. From this relationship, it is understood that the time is the integral of the inverse velocity, $1/v$, or slowness, p, from the source to the receiver as shown in Eq. (1) [29]:

$$v = \frac{d}{t} \rightarrow vt = d, \tag{1}$$

$$t = \int_S^R \frac{1}{v}\,\mathrm{d}l = \int_S^R p\,\mathrm{d}l, \tag{2}$$

$$t_i = \sum_{j=1}^{M} p_j d_{ij} \qquad (i = 1, \ldots, N), \tag{3}$$

where v is the velocity (m/s), d is the distance (m), t is the travel time (s), p is the slowness (s/m), N is the total number of rays, and M is the number of voxels [1].

The microseismic event location and subsequent raypath are calculated using an initial velocity model to represent the rock mass. The velocity model is developed from measured data and allows for calculation of the distance and travel time along the raypath. However, the velocity, distance, and time in an individual voxel or grid cell are not known. Although the distance in each grid cell can be readily solved, the time and velocity are still unknown. Arranging the time, distance, and slowness for each voxel into matrices, the velocity can be determined through inverse theory as shown in Eq. (4) [29]:

$$\mathbf{T} = \mathbf{DP} \rightarrow \mathbf{P} = \mathbf{D}^{-1}\mathbf{T}, \tag{4}$$

where $\mathbf{T}$ is the travel time per ray matrix ($1 \times N$), t_i is the travel time of the ith ray, $\mathbf{D}$ is the distance per ray per voxel matrix ($N \times M$), d_{ij} is the distance of the ith ray in the jth voxel, $\mathbf{P}$ is the slowness per grid cell matrix ($1 \times M$), and p_j is the slowness of the jth voxel.

Usually, the inverse problem is either underdetermined (more voxels than rays), or overdetermined (more rays than voxels) [22,30,31]. The most effective way to solve this problem is by an iterative process.

3. Case study

3.1. Site characteristics

Data for this study were collected between July 7, 1997 and August 8, 1997, at an underground coal mine in the western United States. The mine employs longwall mining, and has produced an average of 7.5 million tons per year between 1995 and 2004 [32]. The coal seam ranges in thickness from 2.6 to 3.0 m (8.5–9.8 ft) with a depth of approximately 350 m (1150 ft). The mine operates longwall panels that are approximately 5490 m (17,980 ft) long and 250 m (815 ft) wide. Over the course of the study, the face advanced 431 m (1415 ft), averaging about 24 m (79 ft) per day. Sixteen geophones were assembled on the surface to monitor and locate microseismic events. Fig. 1 displays a plan view of the geophone locations over the portion of the longwall panel of interest. The geophones provide adequate spatial coverage of the entire area of study.

3.2. Inversion parameters

The data were analyzed using *GeoTOM*, a commercial program that generates tomograms through the simultaneous iterative reconstructive technique (SIRT) [33]. SIRT is an appropriate algorithm because the solution tends to both converge and diverge slowly, so that the solution is relatively stable [33,34]. A voxel size of 15 m per side (approximately 50 ft per side) was input into the program. This voxel size was determined to be sufficiently small to ascertain the general stress trend, but sufficiently large that artifacts would not disrupt interpretation of the tomogram. Ideal voxel size has an edge length equal to the typical wavelength of the rays [21], and at the smallest half of the typical wavelength [18]. The average p-wave velocity for this data set is 3600 m/s (12,000 ft/s) with a typical frequency content of 30 Hz, indicating a wavelength of 120 m and, therefore, ideal voxel size of 120 m. This voxel size would not adequately delineate expected velocity features. Many of the 15 m voxels are traversed by over 1000 rays, so they are well constrained. However, by decreasing the voxel size there is a risk of creating artifacts in the model. Artifacts are broadly defined as an error in the reconstructed image due to an inaccuracy of measurement [35] or velocity anomalies that have been displaced relative to their proper locations [36]. In this case, artifacts are velocity anomalies that do not represent a physical state or structure in the model, and they may occur in areas of the model where ray coverage is poor. The inversion algorithm assigns these abnormally high or low velocities as it attempts to fit the model to the data. In order to decrease the voxel size without creating artifacts, velocities for voxels that were not traversed by any rays were removed from the results. The remaining data were input into a three-dimensional modeling program, and the missing values were assigned based on the nearest voxels, using an inverse distance algorithm. Straight raypaths for day 18 of the study are displayed in Fig. 2.

Additional input parameters, including an initial velocity model, anisotropy, smoothing, and the number of curved and straight ray iterations to be performed, were required. An initial velocity model is a three-dimensional model of

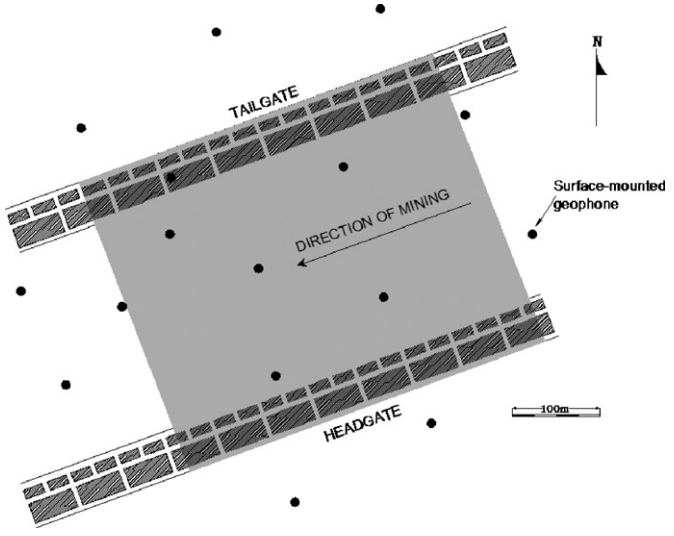

Fig. 1. Plan view of the area under study. The gray area indicates total area mined over 18 days of study.

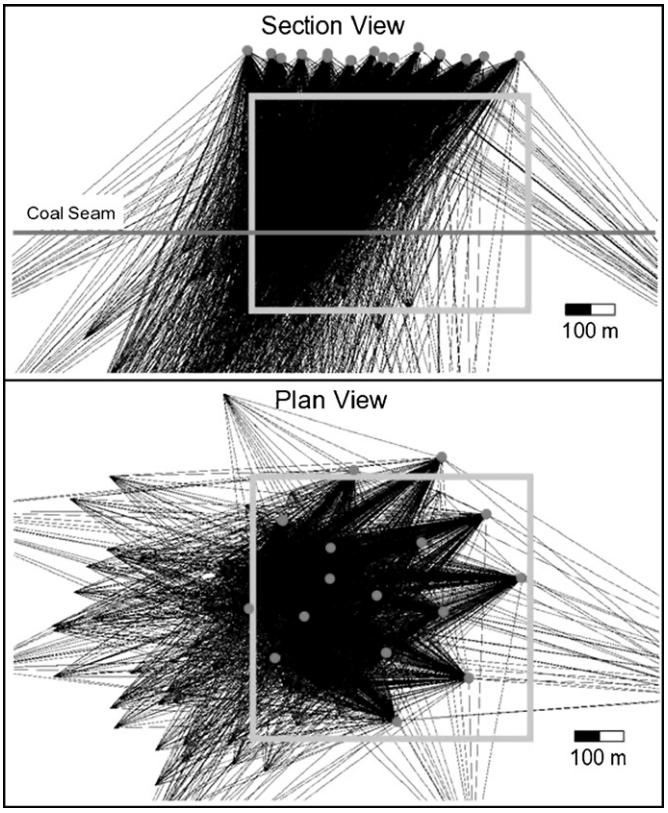

Fig. 2. Straight raypaths for day 18 of the study. The side view (top) shows the area of interest outlined in gray, with the geophones located on the surface in gray and the location of the coal seam plotted in dark gray. The plan view (bottom) shows the area of interest outlined in gray, with the geophone locations in gray.

the p-wave velocity of the rock mass based on geophysical data that has been previously collected. SIRT is an iterative technique; the algorithm must have an initial velocity value to perturb the first iteration. The initial velocity model allows the inversion to be calculated more efficiently and accurately. The initial velocity model was provided with the raw data from National Institute for Occupational Safety and Health (NIOSH), and a one-dimensional interpretation of the model is displayed in Fig. 3.

Anisotropy refers to the variation of a characteristic of a material with the direction of measurement [37]. In this situation, anisotropy refers to the variation in p-wave velocity as measured parallel or perpendicular to the bedding layers. Both the direction and magnitude of the anisotropy were inputted. The anisotropy vector is taken to be normal to the dipping layers of the initial velocity model and is [−0.068, 0.057, 0.996], as provided by NIOSH. The anisotropy magnitude refers to the ratio of the velocity measured orthogonally to the anisotropy vector to the velocity that has been measured parallel to the anisotropy vector. The magnitude of anisotropy was determined experimentally by inverting the data with anisotropy magnitudes varying from 0.8 to 1.2, with the goal of minimizing the travel time residuals resulting from the inversion. An anisotropy magnitude of 1.1 minimized the residuals, indicating that this value improves the model so that it better fits the data. This value indicates that the velocity along the seismic ray is 1.1 times faster when the ray is oriented orthogonal to the anisotropy vector as opposed to when the ray is parallel to the vector. An anisotropy magnitude of 1.1 is reasonable as Cox states that published values generally range from 1.0 to 1.45 [38].

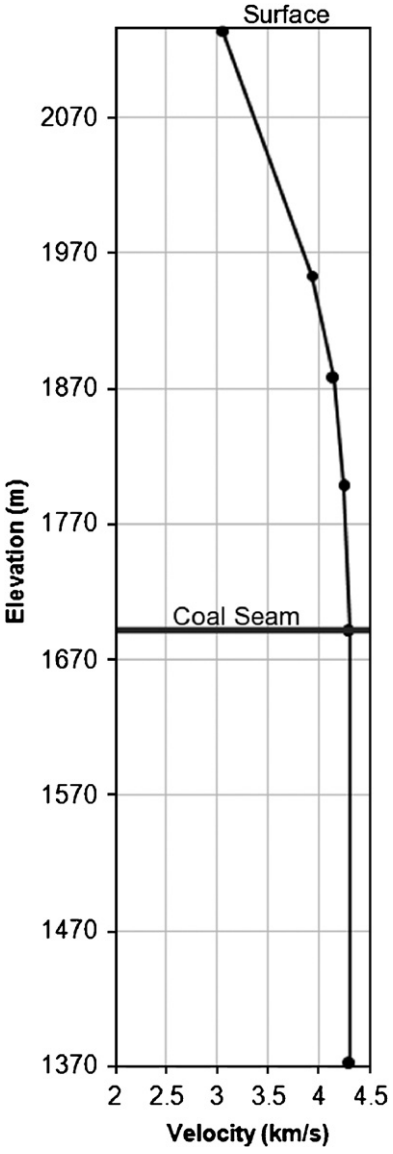

Fig. 3. Initial velocity model. The coal seam is displayed in black at approximately 1700 m. The model is layered normal to the given anisotropy vector.

Tomographic inversions were performed assuming both straight and curved raypaths. The straight ray calculation is simply the straight line distance between the source and the receiver, while the curved ray calculation allows for ray bending according to Snell's Law. Snell's Law implies that for the layered initial velocity model the straight ray assumption is not valid. However, the root-mean-square travel time residuals were actually smaller for the straight ray assumption than for the curved ray assumption, while the sum of the residuals were significantly smaller for the curved ray assumption. The sum of the residuals is simply the sum of the travel time residuals for each ray in the iteration and is not a measure of the magnitude of the residuals, but rather of their distribution about zero. The higher sum of the residuals for the straight ray assumption indicates that the straight ray algorithm consistently underestimates the raypath length. Clement and Knoll generated synthetic tomograms for cross borehole data with straight and curved ray algorithms and found similar results in their tests; the root-mean-square error was smaller for the straight ray algorithm than for the curved ray algorithm. They still concluded that the curved ray algorithm was favorable because it more accurately portrayed their model [39]. By the same logic, it was determined that the curved ray assumption was appropriate for this data, and each tomogram was generated with 10 curved ray iterations.

A smoothing constant was applied in all directions. Smoothing replaces the velocity value at a node by a weighted average of the velocity at that node and the surrounding nodes. Smoothing can help to remove inconsistencies in the model, but if a model is oversmoothed important anomalies can be removed. A fairly small smoothing constant of 0.02 was applied to surrounding nodes in order to avoid oversmoothing.

4. Results

4.1. Abutment stress

Major stress features resulting from abutment stress were expected to be imaged through velocity tomography.

Abutment stress is a result of stress redistribution due to the extraction of ore, and occurs along or near the boundary where material has been removed [40]. An undisturbed coal seam with competent roof and floor strata will have a fairly uniform stress distribution. As coal is removed this distribution is disrupted and the load shifts to another intact area. In longwall mining, this stress is transferred immediately in front of the face, and to the sides of the panel (headgate and tailgate). Failure of the roof strata behind the longwall shields is termed the 'gob' and allows for pressure relief.

Very competent strata above a longwall system, such as massive sandstone, may not cave immediately, contributing to extremely high abutment stress in front of the face which can result in rockbursts at the face, and damage to shields due to dynamic loading [41]. The exact distribution of the abutment load is dependent upon the properties of the roof strata and the mining geometry, but abutment stress is usually the largest on the tailgate, if it is adjacent to a previously mined out panel. Front abutment pressure is detectable at a lateral distance ahead of the face approximately equal to the overburden depth, and typically reaches a maximum at a distance of one-tenth the overburden depth. In weak roof, maximum abutment stress along the faceline occurs at the headgate and tailgate corners, but in more competent roof a peak may occur mid-face, depending upon the face length [41]. In addition to vertical stress redistribution, joints, faults, inhomogeneous layering, and horizontal stress orientation may contribute to larger abutment stresses and more erratic failure. Even in optimum conditions roof failure behind longwall shields is rarely uniform [42].

4.2. Velocity tomograms and comparison to numerical modeling

Tomograms were generated for each of the 18 days of the study. Six of these images are presented in Fig. 4. Three-dimensional tomograms were generated, and then sliced laterally at seam level, at an elevation of approximately 1690 m. Plan views for days 2, 5, 7, 12, 15, 18 are displayed with the mining geometry overlain onto the tomogram. In these images, three distinct features can be observed. First, a high-velocity region is identifiable immediately in front of the face for each of the days of the study. Second, a high-velocity region is visible to varying degrees running from the active face down the tailgate alongside the gob. Both of these regions are areas where high abutment stress is expected. Finally, a low-velocity feature moves in conjunction with the face in the location of the gob, as expected.

In order to validate the behavior observed on the tomograms, a simple numerical model of the panel was generated to observe expected vertical stress. The *LAMODEL* (Laminate Model) program was utilized due to its relative ease of use and specific application to tabular deposits. *LAMODEL* is a boundary element, displacement–discontinuity routine that calculates stress for tabular seams. It simulates the overburden as a stack of homogenous isotropic layers with the same Poisson's ratio, Young's modulus, and frictionless interfaces [43]. In Fig. 5, the *LAMODEL* plot for day 18 of the study is displayed alongside the tomogram for the same day. Many of the same features are evident. Additionally, Fig. 6 shows the *LAMODEL* stress distribution as a wireframe plot that emphasizes the relatively higher stress predicted on the tailgate.

5. Conclusions

The tomograms generated from the 18-day study produced repeatable high-velocity features in areas that typically exhibit high stress on longwall panels and in areas that numerical modeling predicts will encounter high stress, including a high-velocity region that is consistently present immediately ahead of the active face and a high-velocity region that is visible along the tailgate side of the panel. Also, these regions are observed to redistribute with longwall face retreat. The tomograms do not display the same degree of resolution as the *LAMODEL* stress plots, and velocity patterns corresponding with individual pillars cannot be ascertained.

While the velocity distribution shown on the tomograms is not as uniform as the stress distribution displayed in the *LAMODEL* plots, true stress redistribution is rarely perfectly uniform due to inhomogeneity in both geologic properties and fracture and deformation. Additionally, the *LAMODEL* plots display more specific stress details. Stress on each of the headgate and tailgate pillars is identifiable, while no such detail is visible on the velocity tomograms. One reason for the lack of detail on the tomograms may be insufficient ray coverage. While the mining-induced microseismic events are ideal for long-term sources they do not provide the dense and uniform ray coverage provided by active sources. Also, the nature of the velocity–stress relationship causes some ambiguity in the image. In rocks with high elastic moduli stress increase may not translate to high p-wave velocity, so while differences in high-stress regions are discernible on the *LAMODEL* plots, they are not discernible on the velocity tomograms.

Several improvements can be made to this method to provide better information about the state of stress in the rock mass including implementation of attenuation tomography, double difference tomography, and adaptive mesh. Attenuation tomography could provide additional information about the degree of fracture in the rock mass, while double difference tomography and the application of an adaptive mesh could assist with some of the challenges of passive source implementation. Double difference tomography combines the inversion of the velocity data with the location of the microseismic events, optimizing both [44]. Adaptive mesh tomography allows for variation in voxel size to account for nonuniform ray coverage [45]. Additionally, quantification of uncertainty will be addressed in

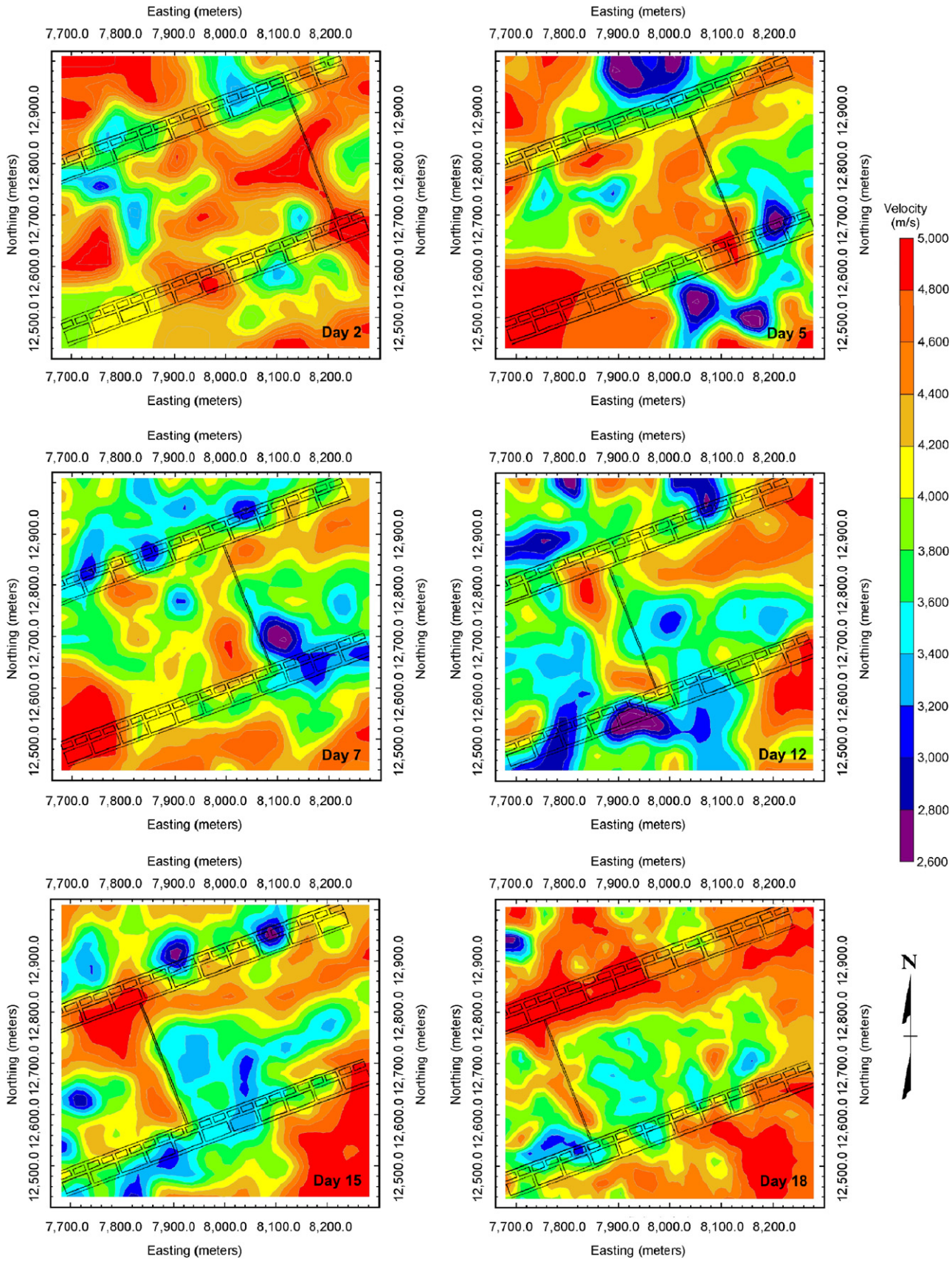

Fig. 4. Plan view velocity tomograms at seam level, $z = 4695$ m. Days 2, 5, 7, 12, 15, and 18 of the study are shown. The face is retreating in the southwest direction.

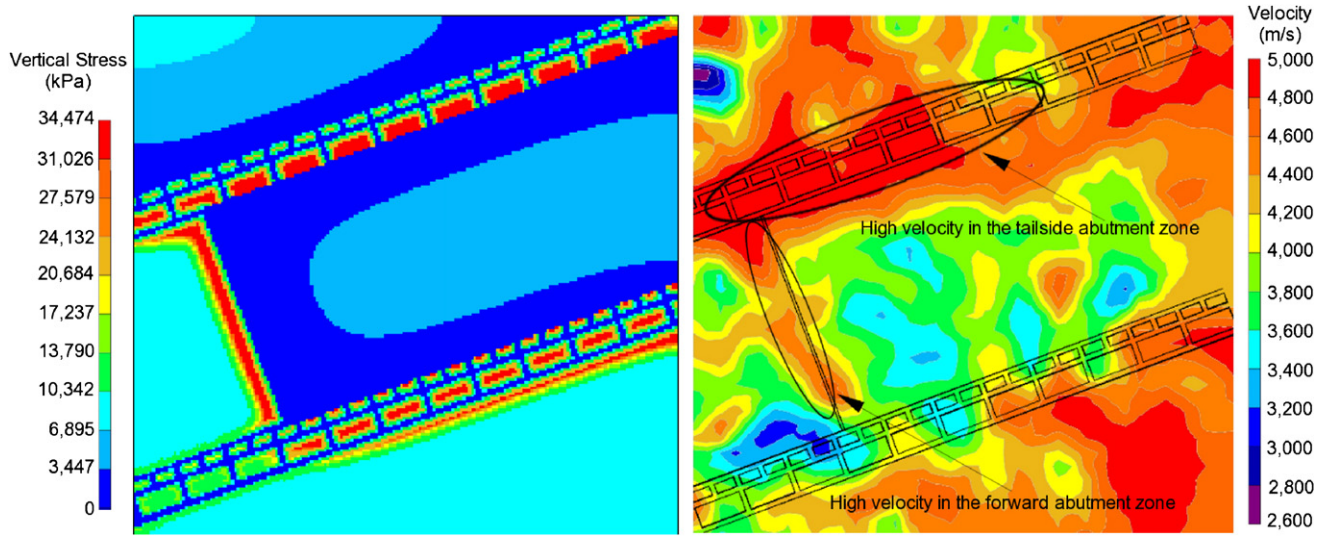

Fig. 5. *LAMODEL* stress plot (left) and velocity tomogram (right), plan view at seam level, $z = -695$ m, for day 18. High-velocity areas corresponding to the forward abutment and tailgate side abutment zones are circled.

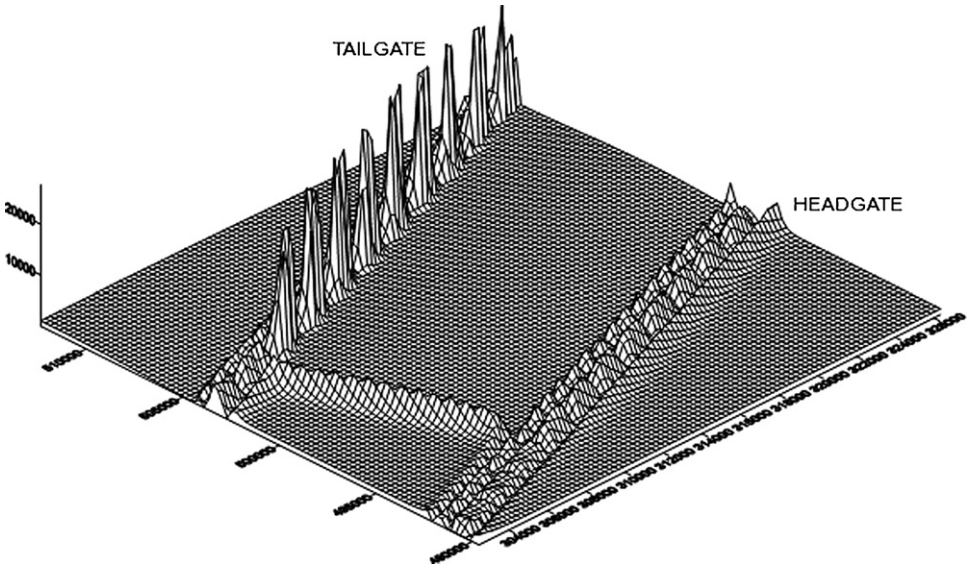

Fig. 6. *LAMODEL* wireframe stress plot, illustrating the relatively higher stress predicted on the tailgate side of the panel, along with the front abutment stress.

future studies. By applying these techniques in concert, time-lapse tomographic images of velocity distributions in underground mines can be improved and utilized for noninvasive examination of stress redistribution in a rock mass, thereby increasing the safety and efficiency of the mining process.

Acknowledgments

The authors are grateful to the National Institute for Occupational Safety and Health for providing the raw data for this study. This research was funded by a National Science Foundation CAREER Grant (CMS-0134034).

References

[1] MSHA. Fatalities year-to-date: coal, 〈http://www.msha.gov/fatals/fabc.htm〉; 2006 [accessed 12.04.06].
[2] Bräuner G. Rockbursts in coal mines and their prevention. Rotterdam: Balkema; 1994.
[3] Ellenberger JL, Heasley KA. Coal mine seismicity and bumps: historical case studies and current field activity. In: Proceedings of the 19th international conference ground control in mining, Morgantown, WV, 2000. p. 112–20.
[4] Wyllie MRJ, Gregory AR, Gardner GHF. An experimental investigation of factors affecting elastic wave velocities in porous media. Geophysics 1958;23:459–93.
[5] Thill RE. Acoustic methods for monitoring failure in rock. In: Proceedings of the 14th US symposium on rock mechanics, University Park, PA, 1973. p. 649–87.

[6] Toksöz MN, Cheng CH, Timur A. Velocities of seismic waves in porous rocks. Geophysics 1976;41:621–45.
[7] Seya K, Suzuki I, Fujiwara H. The change in ultrasonic wave velocities in triaxially stress brittle rock. J Phys Earth 1979;27:409–21.
[8] Young RP, Maxwell SC. Seismic characterization of a highly stressed rock mass using tomographic imaging and induced seismicity. J Geophys Res 1992;97:12361–73.
[9] Eneva M, Mendecki AJ, Van Aswegen G. Seismic response of rock mass to blasting and rockburst potential. Int J Rock Mech Min Sci 1998;35:390–1.
[10] Iannacchione A, Bajpayee TS, Edwards J. Forecasting roof falls with monitoring technologies—a look at the Moonee Colliery experience. In: Proceedings of the 24th international conference ground control in mining, Morgantown, WV, 2005. p. 44–60.
[11] Eneva M, Van Aswegen G, Mendecki AJ. Volume of ground motion and seismic hazard. Int J Rock Mech Min Sci 1998;35:393–4.
[12] Herman GT. Image reconstruction from projections: the fundamentals of computerized tomography. New York: Academic Press; 1980.
[13] Rafat G, Lehmann B, Toumani A, Rueter H. Characterization of rock ahead and around tunnels and boreholes by use of geophysical and geological methods. Int J Rock Mech Min Sci 2001;38:903–8.
[14] Greenhalgh S, Zhou B, Cao S. A crosswell seismic experiment for nickel sulphide exploration. J Appl Geophys 2003;53:77–89.
[15] Young RP, Hutchins DA, Talebi S, Chow T, Falls S, Farrell L, et al. Laboratory and field investigations of rockburst phenomena using concurrent geotomographic imaging and acoustic emission/microseismic techniques. Pure Appl Geophys 1989;129:647–59.
[16] Prasad M, Manghnani MH. Effects of pore and differential pressure on compressional wave velocity and quality factor in Berea and Michigan sandstones. Geophysics 1997;62:1163–76.
[17] Meglis IL, Chow T, Martin CD, Young RP. Assessing in situ microcrack damage using ultrasonic velocity tomography. Int J Rock Mech Min Sci 2004;42:25–34.
[18] Friedel MJ, Jackson MJ, Williams EM, Olson MS, Westman E. Tomographic imaging of coal pillar conditions: observations and implications. Int J Rock Mech Min Sci Geomech Abstr 1996;33:279–90.
[19] Scott DF, Girard JM, Williams TJ, Denton DK. Comparison of seismic tomography, strain relief, and ultrasonic velocity measurements to evaluate stress in an underground pillar. In: Proceedings of society for mining metallurgy and exploration annual meeting, Denver, 1999.
[20] Scott DF, Williams TJ, Tesarik D, Denton DK, Knoll SJ, Jordan J. Geophysical methods to detect stress in underground mines. NIOSH, Rep Invest 9661, 2004.
[21] Watanabe T, Sassa K. Seismic attenuation tomography and its application to rock mass evaluation. Int J Rock Mech Min Sci 1996;33:467–77.
[22] Manthei G. Seismic tomography on a pillar in a potash mine. In: Proceedings of the 4th international symposium rockbursts and seismicity in mines, Krakow, 1997. p. 237–42.
[23] Maxwell SC, Young RP. A controlled in-situ investigation of the relationship between stress, velocity and induced seismicity. Geophys Res Lett 1995;22:1049–52.
[24] Maxwell SC, Young RP. Seismic imaging of rock mass responses to excavation. Int J Rock Mech Min Sci Geomech Abstr 1996;33:713–24.
[25] Körmendi A, Bodoky T, Hermann L, Dianiska L, Kálmán T. Seismic measurements for safety in mines. Geophys Prospect 1986;34:1022–37.
[26] Maxwell SC, Young RP. A comparison between controlled source and passive source velocity images. Bull Seism Soc Am 1993;83:1813–34.
[27] Friedel MJ, Scott DF, Williams TJ. Temporal imaging of mine-induced stress change using seismic tomography. Eng Geol 1997;46:131–41.
[28] Westman EC, Haramy KY, Rock AD. Seismic tomography for longwall stress analysis. In: Proceedings of the 15th international conference ground control in mining, Golden, CO, 1996.
[29] Jackson MJ, Tweeton DR. MIGRATOM: geophysical tomography using wavefront migration and fuzzy constraints. US Bur Mines Rep Invest 9497, 1994.
[30] Tarantola A. Inverse problem theory: methods for data fitting and model parameter estimation. New York: Elsevier; 1987.
[31] Menke W. Geophysical data analysis: discrete inverse theory. 2nd ed. San Diego: Harcourt Brace Jovanovich; 1987.
[32] MSHA. Data retrieval system, 〈http://www.msha.gov/drs/drshome.htm〉; 2005 [accessed 05.10.05].
[33] Dines KA, Lytle RJ. Computerized geophysical tomography. Proc IEEE 1979;67:1065–74.
[34] Gilbert P. Iterative methods for the three-dimensional reconstruction of an object from projects. J Theor Biol 1972;36:105–17.
[35] Hsieh J. Computed tomography: principles, design, artifacts, and recent advances. Bellingham, WA: SPIE Optical Engineering Press; 2003.
[36] Iyer HM, Hirahara K. Seismic tomography: theory and practice. New York: Chapman & Hall; 1993.
[37] McGraw-Hill dictionary of geology and mineralogy. New York: McGraw-Hill, 2003.
[38] Cox M. Static corrections for seismic reflection surveys. Tulsa: Society of Exploration Geophysicists; 1999.
[39] Clement WP, Knoll, MD. Tomographic inversion of crosshole radar data: confidence in results. In: Proceedings symposium application of geophysics to environmental and engineering problems, Arlington, VA, 2000. p. 553–62.
[40] Peng SS, Chiang HS. Longwall mining. New York: Wiley; 1983.
[41] Haramy KY, Magers JA, McDonnell JP. Mining under strong roof. In: Proceedings of the 7th international conference ground control in mining, Morgantown, WV, 1988. p. 179–94.
[42] Maleki H. The application of geotechnical monitoring to stability evaluation and mine design. In: Proceedings of society for mining metallurgy and exploration annual meeting, Phoenix, 2002.
[43] Heasley KA. LAMODEL, Version 2.1.1, 2005.
[44] Zhang H, Thurber CH. Double-difference tomography: the method and its application to the Hayward Fault, California. Bull Seism Soc Am 2003;93:1875–89.
[45] Grunberg M, Genaud S, Mongenet C. Parallel adaptive mesh coarsening for seismic tomography. In: Proceedings of the 16th symposium computer architecture and high performance computing, 2004. p. 158–65.